chemosensors

MDPI

Article

Luminescent Self-Assembled Monolayer on Gold Nanoparticles: Tuning of Emission According to the Surface Curvature

Angela Candreva [1,2], Giuseppe Di Maio [1], Francesco Parisi [1], Francesca Scarpelli [1], Alessandra Crispini [1], Nicolas Godbert [1], Loredana Ricciardi [2], Antonello Nucera [3], Carmen Rizzuto [3], Riccardo C. Barberi [2,3], Marco Castriota [2,3] and Massimo La Deda [1,2,*]

[1] Department of Chemistry and Chemical Technologies, University of Calabria, 87036 Rende, Italy; angela.candreva@unical.it (A.C.); giuseppe.dimaio@unical.it (G.D.M.); francesco.parisi@unical.it (F.P.); francesca.scarpelli@unical.it (F.S.); a.crispini@unical.it (A.C.); nicolas.godbert@unical.it (N.G.)

[2] Institute of Nanotechnology (NANOTEC), National Research Council (CNR), UOS Cosenza, 87036 Rende, Italy; loredana.ricciardi@cnr.it (L.R.); riccardo.barberi@fis.unical.it (R.C.B.); marco.castriota@fis.unical.it (M.C.)

[3] Department of Physics, University of Calabria, 87036 Rende, Italy; antonello.nucera@unical.it (A.N.); carmen.rizzuto@unical.it (C.R.)

* Correspondence: massimo.ladeda@unical.it

Abstract: Until now, the ability to form a self-assembled monolayer (SAM) on a surface has been investigated according to deposition techniques, which in turn depend on surface-coater interactions. In this paper, we pursued two goals: to form a SAM on a gold nanosurface and to correlate its formation to the nanosurface curvature. To achieve these objectives, gold nanoparticles of different shapes (spheres, rods, and triangles) were functionalized with a luminescent thiolated bipyridine (Bpy-SH), and the SAM formation was studied by investigating the photo-physics of Bpy-SH. We have shown that emission wavelength and excited-state lifetime of Bpy-SH are strongly correlated to the formation of specific aggregates within SAMs, the nature of these aggregates being in close correlation to the shape of the nanoparticles. Micro-Raman spectroscopy investigation was used to test the SERS effect of gold nanoparticles on thiolated bipyridine forming SAMs.

Keywords: self-assembled monolayer; gold nanorods; gold nanotriangles; gold nanospheres; emission spectroscopy; the curvature of nanosurface; SERS

Citation: Candreva, A.; Di Maio, G.; Parisi, F.; Scarpelli, F.; Crispini, A.; Godbert, N.; Ricciardi, L.; Nucera, A.; Rizzuto, C.; Barberi, R.C.; et al. Luminescent Self-Assembled Monolayer on Gold Nanoparticles: Tuning of Emission According to the Surface Curvature. *Chemosensors* **2022**, *10*, 176. https://doi.org/10.3390/chemosensors10050176

Academic Editors: Iole Venditti, Paolo Prosposito and Alessandra Paladini

Received: 4 April 2022
Accepted: 3 May 2022
Published: 6 May 2022

1. Introduction

Self-assembled monolayers (SAMs) are highly ordered organic molecular aggregates with a thickness of a single molecule, i.e., in the range of a few nanometers, chemisorbed on a substrate. SAMs of organic molecules have been the object of a very large number of investigations [1,2] in relation to a wide panel of applications in fields such as corrosion protection [3], biosensors [4], drug-delivery systems [5] and molecular electronics [6]. Specifically regarding SAMs on metal surfaces, many studies have focused on molecules bearing a thiol termination because of the ease of S-metal binding. In particular, alkanethiols, dithiols, thiophenes, and thiophenols on various substrates, such as Au, Ag, Pt, and Cu have been investigated [7–9]. In this regard, dithiol molecules have attracted particular attention owing to the possibility of using the thiol terminations to bind two different metallic entities. A dithiol SAM with free pendent SH groups allows for the grafting of metallic atoms or nanoparticles [10–13] that can, in turn, become a useful platform for the further growth of metallic contacts and more complex heterostructures [14]. In addition, SAMs formed on metallic nanoparticles have attracted a plethora of research efforts due to the possibility of combining the unique properties of nanosized metal clusters with those of ordered organic molecules in a new class of materials, i.e., monolayer-protected metal nanoparticles (MPMNs) [15]. A particularly relevant aspect of nanoparticles is that the

percentage of the total number of interfacial atoms is much greater than in bulk materials. Because the electronic states of interfacial atoms of nanoparticles affect their chemical, optical, and electronic properties, there is a strong synergy between nanoparticles and SAMs [7]. However, the structures of SAMs differ greatly depending on the curvature of a given surface [15]. Unlike SAMs formed on planar macro surfaces, MPMNs offer the possibility of studying the effect of curvature on the formation of monolayers, as it is possible to prepare metal nanoparticles with quite varied shapes, such as spheres, rods, stars, triangles, and cubes—each with a specific surface curvature.

The nanoscale surface curvature exerts a profound effect on the adsorbed molecules–nanoparticles interactions. For this reason, and due to the outstanding relationship between the shape of nanoparticles and the energy of their localized surface plasmon resonance [16] (which in the case of gold is included in the visible spectrum), gold nanoparticles covered with monolayers of thiol-functionalized molecules have been intensively studied, both for their applications and the exploration of phenomena due to the anisotropic surface stress [17]. Indeed, understanding the interface at the nanometer scale is crucial for a wide range of applications of gold nanoparticles such as labeling, sensing, drug delivery, medical therapies, molecular electronics, and catalysis [18]. For this purpose, many different thin-film characterization techniques have been applied to SAMs [2,3,19–21], including microscopy (e.g., STM, AFM), diffraction (e.g., LEED, GIXD, LEAD), and spectroscopy (e.g., SHG, SFG, XPS, RAIRS). All of the aforementioned techniques require the use of sophisticated and expensive instrumentation. However, it is worth noting that many of these techniques can hardly be applied to nanoparticle samples.

On the other hand, molecular luminescence is a formidable tool in a myriad of application fields, including biology, medicine, electronics, analytics, and material sciences [22]. The photophysical properties of an emitter are strongly influenced not only by the environment surrounding the luminophore (i.e., the solvent), but also by intermolecular interactions which become important in a concentrated solution, or more decisively, in a solid or mesophase. In particular, the formation of dimers or multimers in the ground electronic state or excited dimers/multimers (i.e., excimers), can result in different photophysical behavior with respect to the isolated molecule, leading to an increase or conversely, to quenching of the luminescence with the formation of a new emission band, in some cases [23]. Ordered structures of luminophores, such as crystals or liquid crystals or gel, can show emission properties affected by aggregation [24]. Self-assembled structures [25], derived from dissolving emitters in an organized medium (such as liquid crystals [26,27]) or depositing them onto orienting surfaces to form organized films (such as SAMs [28–30]), can show this luminescence tuning. For this reason, photophysical studies of luminescent SAMs can be highly useful to probe the type of aggregates formed within the layer.

Herein, we present the synthesis and photophysical characterization of differently shaped gold nanoparticles (rod, sphere, and triangle) functionalized with 5,5′-bis(mercapto methyl)-2,2′-bipyridine (briefly, Bpy-SH). The photophysical properties of the obtained MPMNs Bpy-SH@AuNR (rod), Bpy-SH@AuNS (sphere), and Bpy-SH@AuNT (triangle) were studied and compared with those of a Bpy-SH monolayer on gold plates (Bpy-SH@Au-plate).

The formation of a self-assembled monolayer on a gold nanosurface has been demonstrated through a deep analysis of luminescence data, revealing a dramatic change of the thiolated bipyridine emission, due to a face-to-face organization of the bipyridine similar to that observed in solid or concentrated solution [31]. Furthermore, the comparison between the luminescence properties of the newly synthesized SAM@AuNP and the shape (spherical, rod-shaped, or triangular) of the gold nanoparticles allowed for correlation between the SAM formation and the nanosurface curvature, providing the first example of a photophysical study of luminescent SAMs on nanoparticles with different shapes.

2. Materials and Methods

All chemicals were purchased from Sigma-Aldrich (Schnelldorf, Germany; highest purity grade available) and used as received.

2.1. Synthesis of Gold Nanorods

The synthesis of gold nanorods capped with cetyltrimethylammonium bromide (CTAB ($AuNR_{CTAB}$)), was conducted in an aqueous solution using the reported seed-mediated method [32,33]. The synthetic steps proceed through physical separation of the nucleation process (seed solution) from the growth process (growth solution), which allows an effective control of the final shape.

Preparation of the seed solution. A total of 25 µL of 5.0×10^{-2} M $HAuCl_4$ water solution was added to 4.7 mL of 0.1 M CTAB water solution and 300 µL of a freshly prepared 1.0×10^{-2} M $NaBH_4$ water solution was then rapidly injected under vigorous stirring. Excess borohydride was consumed by keeping the seed solution for 30 min at room temperature before use.

Preparation of the growth solution. A total of 45 mg of 5-bromosalicylic acid was added to 50 mL of 0.05×10^{-2} M CTAB water solution. After complete dissolution, 480 µL of 1.0×10^{-2} M $AgNO_3$ water solution was added. The solution was mildly stirred for 15 min at room temperature, and then 500 µL of 5.0×10^{-2} M $HAuCl_4$ water solution was added to the mixture. Finally, 130 µL of 0.1 M L-ascorbic acid water solution was added under vigorous stirring, followed by 80 µL of seed solution. After 30 s, the stirring was stopped and the mixture was left undisturbed at room temperature for at least 4 h. The sample was centrifuged to eliminate the unreacted reagents (9000 rpm, 20 min, 30 °C).

Coating agent exchange. CTAB capping agent was replaced with O-(2-mercaptoethyl)-O′-methylpolyethylene glycol (2000 Mn), PEG-SH, by dissolving 30 mg of polymer in 1 mL of deionized water, then adding this solution to 50 mL of 5×10^{-4} M water-dispersed $AuNR_{CTAB}$ [34]. The solution was left stirring overnight. The sample was then centrifuged at 9000 rpm for 30 min and the solid residue dissolved in dichloromethane. Because $AuNR_{CTAB}$ is not soluble in dichloromethane, this induced solubilization is evidence of the successful functionalization of the gold nanorods with PEG-SH, allowed by the formation of a strong sulphur–gold bond. Figure S1 in the Supplementary Materials shows the extinction spectra of the gold nanorods dispersed in solution before and after coating exchange.

Gold nanorods functionalization. A 5,5′-Bis (mercaptomethyl)-2,2′-bipyridine (Bpy-SH) dichloromethane solution (5.5 mL, 1.0×10^{-2} M) was mixed with a dichloromethane solution of $AuNR_{PEG\text{-}SH}$ (50 mL, 5×10^{-4}) and left under stirring for 12 h. As shown below, the formation of an S–Au bond between Bpy-SH and $AuNR_{PEG\text{-}SH}$ guarantees functionalization of the nanoparticles with mercaptomethyl-bipyridine (Bpy-SH@AuNR). Successively, by adding water, two phases were formed. After vigorous stirring, the pink organic phase discolors, while the aqueous phase turns pink due to the migration of the nanorods. PEGylated termination ensures the water solubility of nanorods while free Byp-SH, insoluble in water, remains in the organic phase. The two phases have been separated with a separating funnel and subsequent extractions to ensure the complete removal of the free Bpy-SH from the nanorod solution (thin-layer chromatography of the nanorods solution showed no trace of either labile or free Bpy-SH). Figure 1a shows a TEM image of the obtained Bpy-SH@AuNR nanorods, with an average size of 50×15 nm.

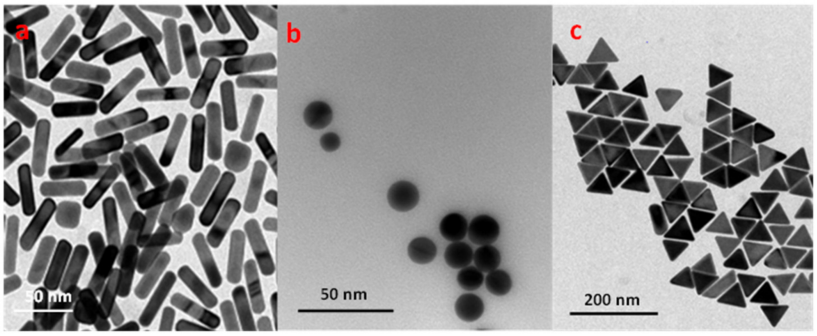

Figure 1. TEM images of Bpy-SH@AuNR (**a**), Bpy-SH@AuNS (**b**) and Bpy-SH@AuNT (**c**).

2.2. Synthesis of Gold Nanospheres

Gold nanospheres, with an average diameter of 18 nm (calculated using the TEM images), covered with sodium citrate ($AuNS_{SC}$) and dispersed in water have been synthesized through a one-step procedure. Sodium citrate (3 mg) was added to 40 mL of cold distilled water with stirring, $HAuCl_4$ water solution (0.020 mL, 0.05 M) was added and after a few minutes, 1.6 mL of a freshly prepared 1.0×10^{-2} M $NaBH_4$ water solution was injected with vigorous stirring. A centrifuge purification to eliminate unreacted reagents was performed. Figure S2 in Supplementary Materials shows the extinction spectrum of the gold nanospheres dispersed in water, where the plasmonic band shows a peak at 522 nm. The coating agent exchange and the functionalization with Bpy-SH of the obtained nano-spheres were achieved exactly as described above for the gold nanorods. Figure 1b reports a TEM image of the obtained Bpy-SH@AuNS nanoparticles.

2.3. Synthesis of Gold Nanotriangles

The synthesis of gold nanotriangles capped with cetyltrimethylammonium chloride (CTAC ($AuNT_{CTAC}$)) was conducted in an aqueous solution using an adaptation of the seed-mediated method [35].

Preparation of the seed solution. A total of 25 µL of 5.0×10^{-2} M $HAuCl_4$ water solution was added to 4.7 mL of 0.1 M CTAC water solution and 300 µL of a freshly prepared 1.0×10^{-2} M $NaBH_4$ water solution was then injected with vigorous stirring. Excess borohydride was consumed by keeping the seed solution at room temperature for 30 min before use.

Preparation of the growth solution. Two growth solutions were prepared, one (A) was used to grow the CTAC-capped seeds into larger nanoparticles; the second (B) was used to direct the anisotropic triangular-shaped growth. Solution A was prepared as follows: 6.4 mL of 0.1 M CTAC water solution was added to 32 mL of water. Subsequently, 160 µL of 5.0×10^{-2} M $HAuCl_4$ water solution was added. Solution B was prepared as follows: 313 mL of 5.0×10^{-2} M CTAC water solution was added to 3.91 mL of 5.0×10^{-2} M $HAuCl_4$ water solution, followed by 2.35 mL of 1×10^{-3} NaI water solution. Then, 160 µL and 3.13 mL of 0.1 M ascorbic acid water solution was added to solutions A and B, respectively, and both solutions were stirred until complete transparency of the solutions was achieved. Finally, 400 µL of 10 times diluted seed solution was added to solution A. At this point, solution A was added to solution B. The obtained dispersion was left undisturbed at room temperature for 2 h. The color, initially intense pink, soon turned into a purple solution containing nanoparticles with different shapes (cubes, spheres, and triangles), as observed by TEM (Figure S3a in Supplementary Materials) and by UV-Vis spectroscopy (Figure S4 in Supplementary Materials). To trigger the selective precipitation of triangles, a water CTAC solution (93.3 mL of 25% w/vol) was added, causing flocculation. After two hours, the supernatant was removed, while the precipitate was redispersed in 5.0×10^{-2} M CTAC water solution, obtaining the desired $AuNT_{CTAC}$ characterized by a blue water solution whose shape was confirmed with TEM (Figure S3c in Supplementary Materials) and UV-Vis spectroscopy (Figure S4, black line, in Supplementary Materials). TEM images and spectroscopic analysis confirm that differently shaped nanoparticles, together with a few triangles, remained in the supernatant (Figures S3b and S4 in Supplementary Materials). The coating agent exchange and the functionalization with Bpy-SH of the obtained nanotriangles were achieved exactly as described above for gold nanorods. Figure 1c reports a TEM image of the obtained Bpy-SH@AuNT nanoparticles, having an average length (along the side) of 50 nm.

2.4. Bpy-SH Covered Gold Plates

A Bpy-SH dichloromethane solution with a concentration of 3.5×10^{-2} M was prepared and degassed with argon. The gold substrate was obtained by thermal evaporation of 200 nm of gold (99.99% purity) onto either polished single crystal silicon (100) wafers primed on freshly cleaved mica at 340 °C. A film of Bpy-SH on the gold plate was deposited

by immersing the gold substrate into the Bpy-SH solution for 6 h at room temperature in the absence of ambient light in a sealed vessel, adapting a reported protocol [36]. Finally, the functionalized gold plate, Bpy-SH@Au-plate, was washed with dichloromethane.

3. Results and Discussion

3.1. Uv-Vis Spectroscopy

The photophysical properties of the investigated samples are reported in Table 1. Since their emission features are attributable to Byp-SH, the electronic transitions of this chromophore in solution will be described first.

Table 1. Photophysical properties of investigated samples.

Sample	Abs, λ/nm (ε/M^{-1} cm^{-1})	Emission Max, λ/nm	Excitation Bands, λ/nm	Lifetime, τ/ns (α/%)	
				at 352 nm	at 418 nm
Bpy-SH@AuNR [a]	273, 300(sh),368, 390(sh), 530, 840 [c]	435	320, 374, 395(sh)	1.6 (94.3), 11.1 (5.7)	0.7 (75.4), 5.2 (24.6)
Bpy-SH@AuNS [a]	291, 520 [c]	350	265	1.5 (79.3), 7.6 (20.7)	
Bpy-SH@AuNT [a]	294, 350(sh), 653 [c]	410	265, 382		0.7 (82.5), 2.4 (17.5)
"diluted" Bpy-SH solution (1.3×10^{-5} M) [b]	254 (15145), 295 (29355), 310 (20300, sh), 330 (1470, sh)	356	270	2.2 (40.2), 7.9 (59.8)	
"concentrated" Bpy-SH solution (3.5×10^{-2} M) [b]	Too intense	418	362		0.9 (81.5), 3.0 (18.5)
Solid Bpy-SH	Not available	435	397		0.7 (86.0), 2.7 (14.0)
Bpy-SH@Au-plate	Not available	435	280, 361		0.6 (5.5), 0.9 (94.5)

[a] Water solution. [b] Dichloromethane solution. [c] The molar extinction coefficient is not defined for the extinction spectrum where electronic transitions are present along with plasmonic resonances. sh = shoulder.

The absorption spectrum of the diluted Bpy-SH dichloromethane solution (1.3×10^{-5} M) is reported in Figure S5 of the Supplementary Materials. It shows two principal peaks at 254 and 295 nm (with a series of shoulders) due to aromatic ππ* transitions, and a weak band at approximately 330 nm, attributed to a symmetry forbidden nπ* transition involving the sulfur atom. In the absorption spectrum of an analogous solution of 2,2′-bipyridine, this band is absent (See Figure S6 in Supplementary Materials), which confirms this attribution. The deactivation originates from a mixed nπ*-ππ* singlet state giving an asymmetric and unstructured emission band at 352 nm (Figure 2); its intensity decay kinetics were deconvoluted with a biexponential function, providing lifetime values of 7.9 and 2.2 ns (with pre-exponential factors of 0.60 and 0.40, respectively). By increasing the concentration, the emission spectrum showed new features (Figure S7 in Supplementary Materials): the 352 nm emission band underwent a bathochromic shift up to 370 nm, and new emission structured peaks were detected at 396, 422, and 485 nm, becoming gradually more evident as the concentration increased. These new peaks can be attributed to the continuous formation of ππ-aggregates, which takes place in the ground electronic state, as can be inferred by comparison of the ground-state spectral patterns (i.e., the absorption spectrum of dilute Bpy-SH in Figure S5, and the excitation spectrum of concentrated Bpy-SH in Figure 2) of diluted and concentrated Bpy-SH to the emission spectral patterns: differences were observed in both cases, confirming aggregation in the ground state [22]. Very interestingly, by diluting the concentrated solutions, the shape of the emission spectrum was restored; thus, it confirms that these spectral variations are not due to the creation of new covalent species but to the formation of ππ-aggregates. The emission spectrum of a highly concentrated solution (3.5×10^{-2} M), reported in Figure 2, clearly shows the disappearance of the 356 nm band, attributed to the isolated Bpy-SH, and well-defined bands at 396 and 418 nm (with weak shoulders at around 445 and 485 nm) attributed to the π-aggregates.

Comparing the excitation spectrum of the diluted solution with that of the concentrated solution, it is evident that Bpy-SH molecules in the concentrated solution were aggregated (the weak band at 273 nm in the excitation spectrum of the concentrated solution is due to a small fraction of non-aggregated bipyridine). The absorption spectrum of the concentrated solution was not collected due to the high concentration. Emission spectrum of the concentrated solution as recorded by excitation at 273 nm gave a negligible emission. The intensity decay kinetics were deconvoluted with a biexponential function, giving lifetime values of 3.0 and 0.9 ns (with pre-exponential factors of 0.18 and 0.82, respectively), considerably shorter than those measured in a diluted solution.

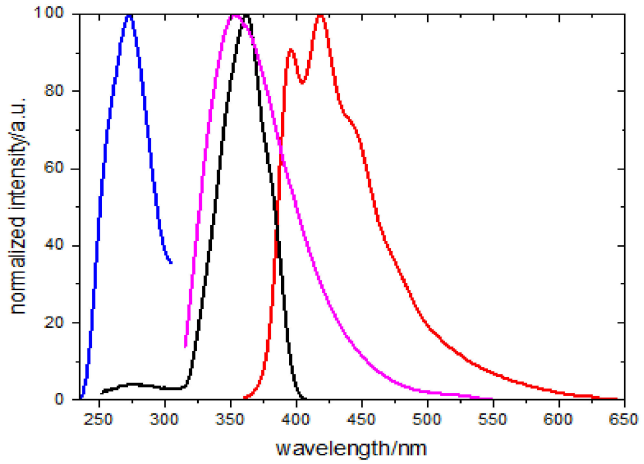

Figure 2. Excitation (λ_{em} = 356 nm, blue line) and emission (λ_{ex} = 270 nm, magenta line) spectra of Bpy-SH in diluted dichloromethane solution (1.3×10^{-5} M). Excitation (λ_{em} = 418 nm, black line) and emission (λ_{ex} = 362 nm, red line) spectra of Bpy-SH in concentrated dichloromethane solution (3.5×10^{-2} M).

The aggregate formation was confirmed by comparing the emission and excitation spectra of the concentrated solution with those of a powder sample (Figure 3). The maxima of the luminescence spectra (λ_{em}^{max} = 435 nm; λ_{ex}^{max} = 397 nm) and their shape gave evidence of the presence of aggregates both in the solid sample and in the concentrated solution.

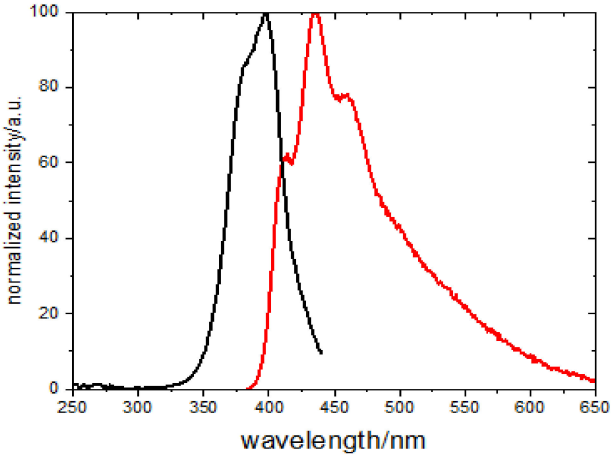

Figure 3. Excitation (λ_{em} = 435 nm, black line) and emission (λ_{ex} = 370 nm, red line) spectra of Bpy-SH in powder sample.

Lifetime values measured in solid (2.7 and 0.7 ns) are almost identical to those measured in the concentrated solution (Table 1) and considerably lower than those measured in the diluted solution, confirming that the formation of π–π stacking interactions between bipyridine molecules results in a faster radiative deactivation, stabilizing the energy levels

of the excited states and reducing the radiative rate constant. After carefully examining the photophysics of Bpy-SH, we will now illustrate and discuss the properties of gold nanoparticles functionalized with this chromophore. Starting from the nanorods Bpy-SH@AuNR, the absorption spectrum they display once dispersed in water is reported in Figure 4, while Figure 5 shows the relative excitation and emission spectra.

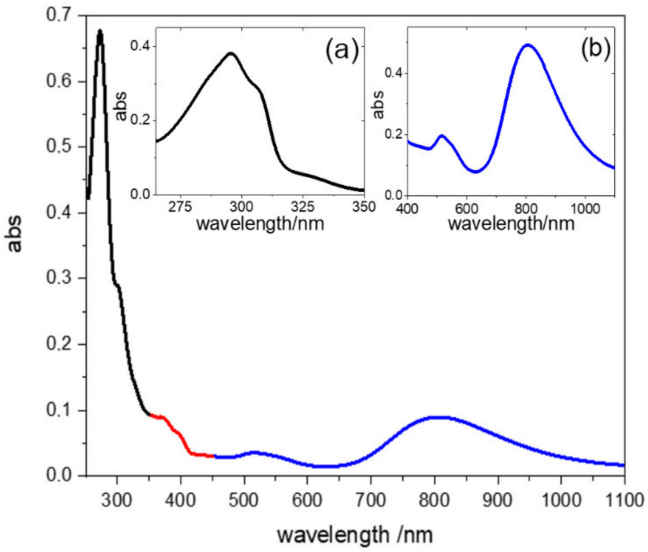

Figure 4. The absorption spectrum of Bpy-SH@AuNR in water solution. The three spectral zones are drawn in different colors: bands attributed to the isolated Bpy-SH transitions (black line), bands attributed to the aggregated Bpy-SH transitions (red line), bands due to the plasmonic resonances (blue line). Subfigure (**a**): absorption spectrum of diluted Bpy, see Figure S5 in Supplementary Materials; Subfigure (**b**): extinction spectrum of Bpy-SH@AuNR. The absorption spectrum of the concentrated solution was not collected due to the high concentration.

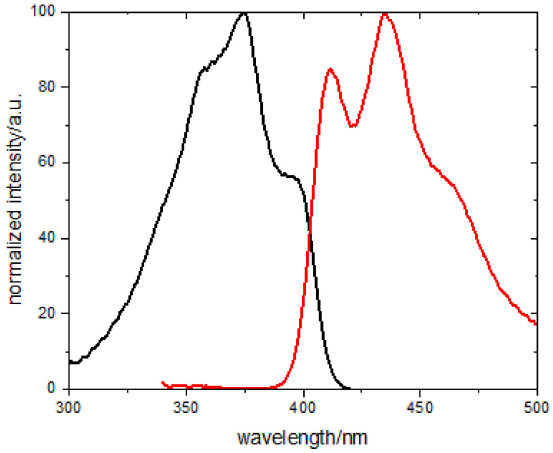

Figure 5. Excitation (λ_{em} = 435 nm, black line) and emission (λ_{ex} = 325 nm, red line) spectra of Bpy-SH@AuNR in water solution.

In the absorption spectrum, several bands are present due to the plasmon resonance of the nanorods and relative to the Bpy-SH molecules linked to the nanoparticles. Bands at 840 and 530 nm are due to the longitudinal and transversal plasmonic modes, respectively, while the spectroscopic features below 450 nm suggest the presence of both isolated and aggregated thiolated bipyridines.

In fact, within the range between 450 and 350 nm, a series of maxima (368 nm) and shoulders (at approximately 390 nm) attributable to Bpy-SH aggregates are present (see the excitation spectrum in Figure 2), while between 260 and 350 nm there are bands (at 273 nm

and the shoulder at approximately 300 nm) that can be attributed to the presence of isolated Bpy-SH molecules (see the absorption spectrum in Figure S5 in Supplementary Materials).

The presence of this different organization of Bpy-SH on the gold nanorods surface was corroborated by the examination of the Bpy-SH@AuNR emissive properties. Figure 5 reports the emission spectrum obtained by exciting at 325 nm. We chose to excite at this wavelength to highlight both the weak emission at about 350 nm, typical of isolated Bpy-SH molecules, and the well-structured emission band with a maximum at 435 nm, attributed to Bpy-SH molecules anchored on the metal through a strong S–Au bond [7,11] and stacked together to form a monolayer on the nanoparticle's surface.

The excitation spectrum in Figure 5 (recorded at 435 nm) confirms the identity of the emissive species; in fact, a comparison to the analogous spectra shown in Figures 2 and 3 suggests the presence of stacked chromophores. Figure S8 in Supplementary Materials reports the excitation spectrum of Bpy-SH@AuNR recorded at λ_{em} = 350 nm (i.e., on the emission maximum of the isolated chromophore), confirming the simultaneous presence of this species.

Our hypothesis is illustrated in Scheme 1: the photophysical data highlight both the presence of aggregated and isolated Bpy-SH molecules. This is plausible if we assume that a stacked Bpy-SH monolayer is formed on the gold nanorods' sides, while on the tips these molecules, anchored Bpy-SH molecules, are unable to form any efficient stacking due to the large curvature of the nanosurface, thus behaving as isolated molecules. The lifetime values (Table 1) collected on the emission maximum of the isolated molecule (i.e., at 352 nm) are longer than that of the monolayered stacked molecules (i.e., at 418 nm), upholding this picture. The model proposed herein is also in agreement with the self-assembly properties of Bpy-SH molecules deposited onto the gold surface, as proposed by Hamoudi and Esaulov [10]. Indeed, Bpy-SH molecules mainly constituted of a rigid core made of two consecutive aromatic rings are more likely to stand straight on the gold surface, leaving a free pendant SH group, rather than being anchored from both sides onto the gold surface. This staple-like geometry is indeed highly disfavored for steric hindrance, as the arms-bearing SH functional groups made of only one carbon atom are too short. Moreover, the existence of free SH moieties, which has been previously revealed by XPS measurements [11] is further corroborated by the high solubility of the functionalized nanoparticles in water.

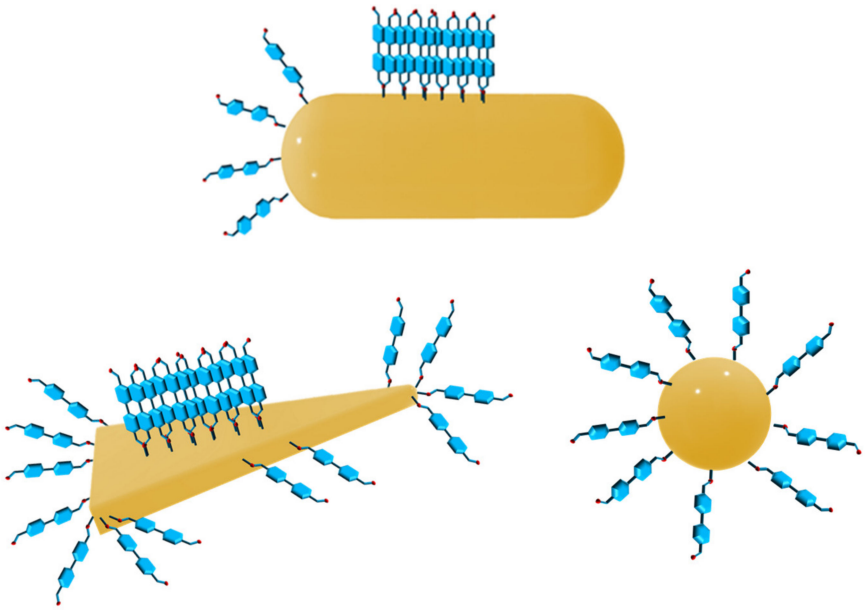

Scheme 1. Schematic representation of Bpy-SH@AuNR, Bpy-SH@AuNT, and Bpy-SH@AuNS (molecules are not in scale). The curvature of the nanosphere is identical to that of the nanorod's tips.

In any case, to further validate our hypothesis, we prepared (see Experimental section) and characterized a Bpy-SH monolayer deposited onto gold substrates (Bipy-SH@Au-plate). Furthermore, to confirm the role of the increased curvature of the tips of the nanorods, we prepared Bpy-SH-functionalized gold nanospheres (Bpy-SH@AuNS) of comparable diameter to the end parts of the nanorods and, finally, to obtain a planar nanosurface with zero curvature, we prepared thiolated bipyridine-functionalized gold nanotriangles (Bpy-SH@AuNT).

Figure 6 reports the emission and excitation spectra of Bipy-SH@Au-plate. The position and shape of the bands and the lifetime value (Table 1) of the monolayered chromophore on the gold surface completely overlap with the data collected from Bpy-SH@AuNR, confirming the formation of SAM onto the sides of the nanorod. Note that the slight differences in the lifetime values are most likely because the nanorods are dispersed in water, while the gold plates are not.

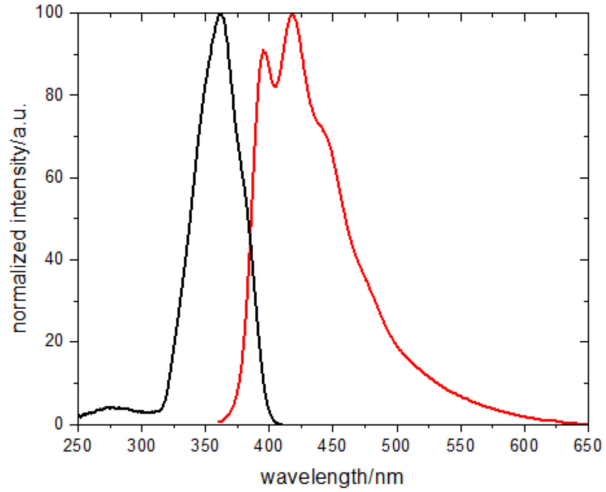

Figure 6. Excitation (λ_{em} = 435 nm, black line) and emission (λ_{ex} = 325 nm, red line) spectra of Bpy-SH@Au-plate.

Photophysical data recorded from the Bpy-SH@AuNS and Bpy-SH@AuNT solutions (Table 1) are of particular interest. The absorption spectrum of Bpy-SH@AuNS (Figure 7) shows a prominent band at 292 nm, due to the $\pi\pi^*$ transition on Bpy-SH, while in the inset, a plasmon resonance band is visible at 520 nm, exactly in the position expected for nanospheres of 18 nm in diameter (see Figure S2 in Supplementary Materials) [37]. Figure 8 reports the absorption spectrum of the gold nanotriangles functionalized with Bpy-SH, namely Bpy-SH@AuNT.

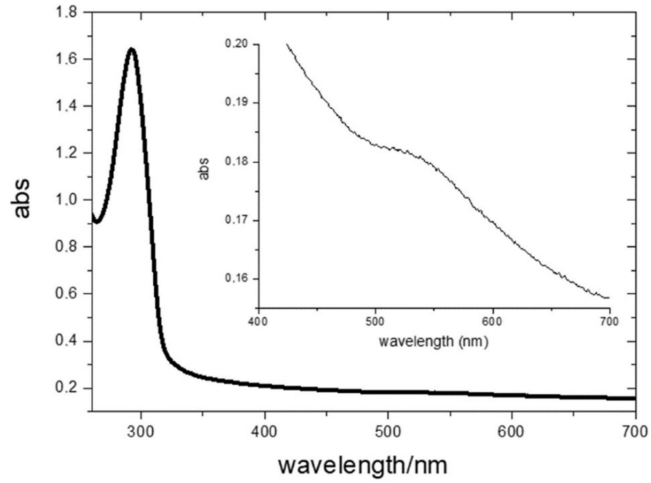

Figure 7. Absorption spectrum of Bpy-SH@AuNS in water solution.

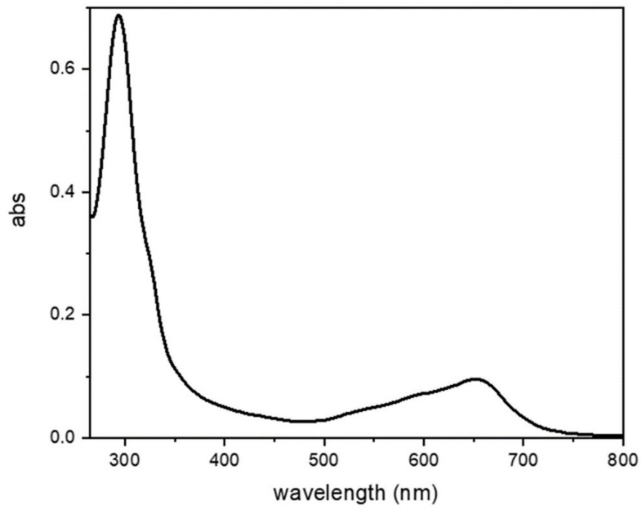

Figure 8. Absorption spectrum of Bpy-SH@AuNT in water solution.

In this spectrum, transitions attributed both to the isolated Bpy-SH molecules (the intense band at 294 nm) and to the aggregated Bpy-SH (the shoulder at about 350 nm) are observed, while the peaks between 550 and 660 are due to the plasmon resonance of the nanoparticles (see Figure S4 in Supplementary Materials). Emission and excitation spectra (Figure 9) of Bpy-SH@AuNS show maxima at 350 and 265 nm, respectively. The measured lifetime values are τ_1 = 1.5 ns and τ_2 = 7.6 ns (Table 1). These data, consistent with the absorption spectrum reported in Figure 7, account for the presence of non-aggregated Bpy-SH molecules on the nanosurface, as expected according to the nanospheres curvature being almost identical to that of the tips of the nanorods (see Scheme 1)

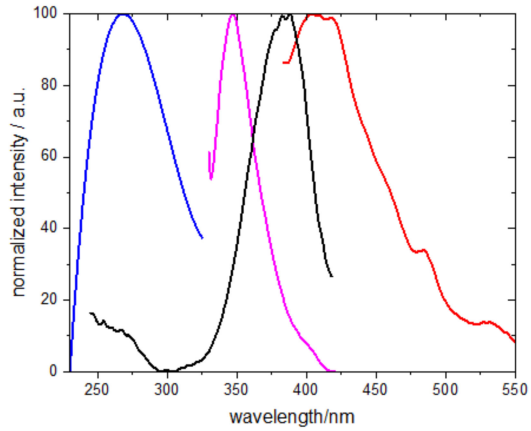

Figure 9. Excitation (λ_{em} = 350 nm, blue line) and emission (λ_{ex} = 265 nm, magenta line) spectra of Bpy-SH@AuNS in water solution. Excitation (λ_{em} = 410 nm, black line) and emission (λ_{ex} = 380 nm, red line) spectra of Bpy-SH@AuNT water solution.

Emission and excitation spectra of Bpy-SH@AuNT, reported in Figure 9, instead show maxima at 418 and 382 nm, respectively, and the measured lifetime values are τ_1 = 0.7 ns and τ_2 = 2.4 ns (Table 1). These values indicate the presence of mostly aggregated Bpy-SH, in line with what was expected, since the nanotriangles' surface has zero curvature, allowing SAM formation (Scheme 1). However, the absorption spectrum (Figure 8) shows not only features attributable to stacked aggregates, but also the presence of isolated Bpy-SH. Indeed, the excitation spectrum of Bpy-SH@AuNT (black line in Figure 9) shows a weak maximum at 265 nm, typical of isolated Byp-SH. The excitation spectrum of Bpy-SH@AuNT was collected at 410 nm, where even the isolated Bpy-SH has a weak emission. Since the Bpy-SH in aqueous solution is not soluble, this band is due to the presence of the chromophore bound on the nanotriangles that is unable to form aggregates.

Nanotriangles are characterized by large flat surfaces (with zero curvature) but have sharp angles at the vertexes (where the radius of curvature becomes very high). These vertexes are highly reactive sites where a high plasmonic field is generated [38]. Therefore, it is plausible to suppose that on the triangle's vertexes Bpy-SH molecules (Scheme 1), due to the largest curvature, are less prompted to form aggregates, and therefore must be responsible for the observed spectral bands.

It is important to note that none of the observed features can be imputed to coupling effects between the chromophore and the gold plasmonic resonance. The emission spectrum of Bpy-SH did not overlap with the plasmonic bands of the nanoparticles in any of the SAM@AuNP samples, excluding energy or electron transfer involved in coupling processes [16,39–42]. The photophysical properties are governed by stacking interactions between the aromatic rings of adjacent molecules; hence, only the shape of the nanoparticles is responsible of the observed differences and must be related exclusively to the type of organization within the SAMs deposited onto the surface of the nanoparticles.

3.2. Raman Spectroscopy

The formation of the SAM by the Bpy-SH on two sample preparations (i.e., Bpy-SH@Au-plate and Bpy-SH@AuNR) was investigated by Raman spectroscopy [43–49]. As a starting reference, the representative Raman spectrum of the thiolated bipyridine (Bpy-SH) powder collected with the laser source at 532 nm is shown in Figure 10. The Raman band attributions are reported in Table S1 in the Supplementary Materials. In the Raman spectra, collected by a laser source at 633 nm, no Raman features were detected and for this reason, relative spectra were not shown.

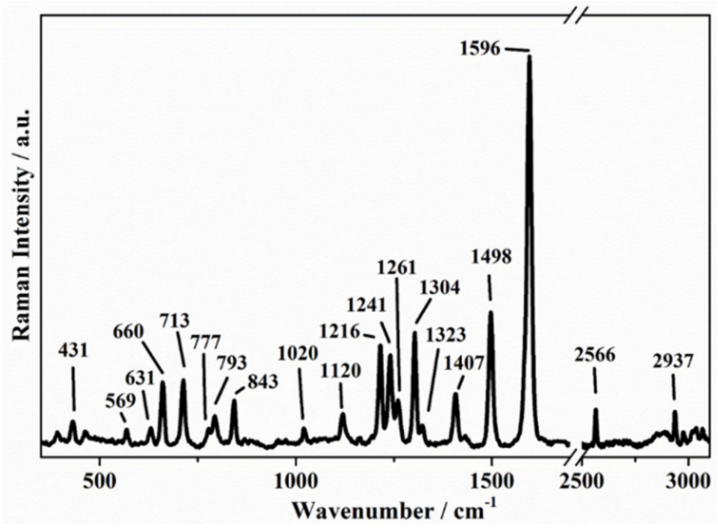

Figure 10. Raman spectrum of Bpy-SH in powder sample collected in the ranges between 350 and 1700 cm^{-1} and between 2500 and 3100 cm^{-1} (laser source at 532 nm).

When Bpy-SH is deposited onto a gold plate [50], a surface-enhanced Raman scattering (SERS) effect is observed. In Figure 11, the two representative SERS spectra collected on the sample Bpy-SH@Au-plate are shown. The first representative SERS spectra is shown in the range between 400 and 1650 cm^{-1} (Figure 11a), while the second representative SERS spectrum is shown in the ranges between 500 and 1100 cm^{-1}, 1170 and 1800 cm^{-1}, and 2450 and 3000 cm^{-1} (Figure 11b,c) [51–54]. The ranges not shown for both the spectra did not present any detectable features. The sharp peaks of Figure 11a that fall at 433, 465, 569, 630, 661, 713, 794, 843, 1022, 1119, 1215, 1240, 1260, 1301, 1321, 1406, 1496, and 1593 cm^{-1} can be assigned by using the modes described in Table S1 in the Supplementary Materials. Such Raman peaks are due to the presence of Bpy-SH. The SERS spectra shown in Figure 11b,c are quite interesting. In this case, the Raman band at 2561 cm^{-1} is assigned

to the S–H bond stretching and the bands at 747 and 1541 cm^{-1} are associated to the ν_5 (CH o.p. bend + ring o.p. def) and ν_2 (ring stret.) mode of Bpy-SH, respectively [55].

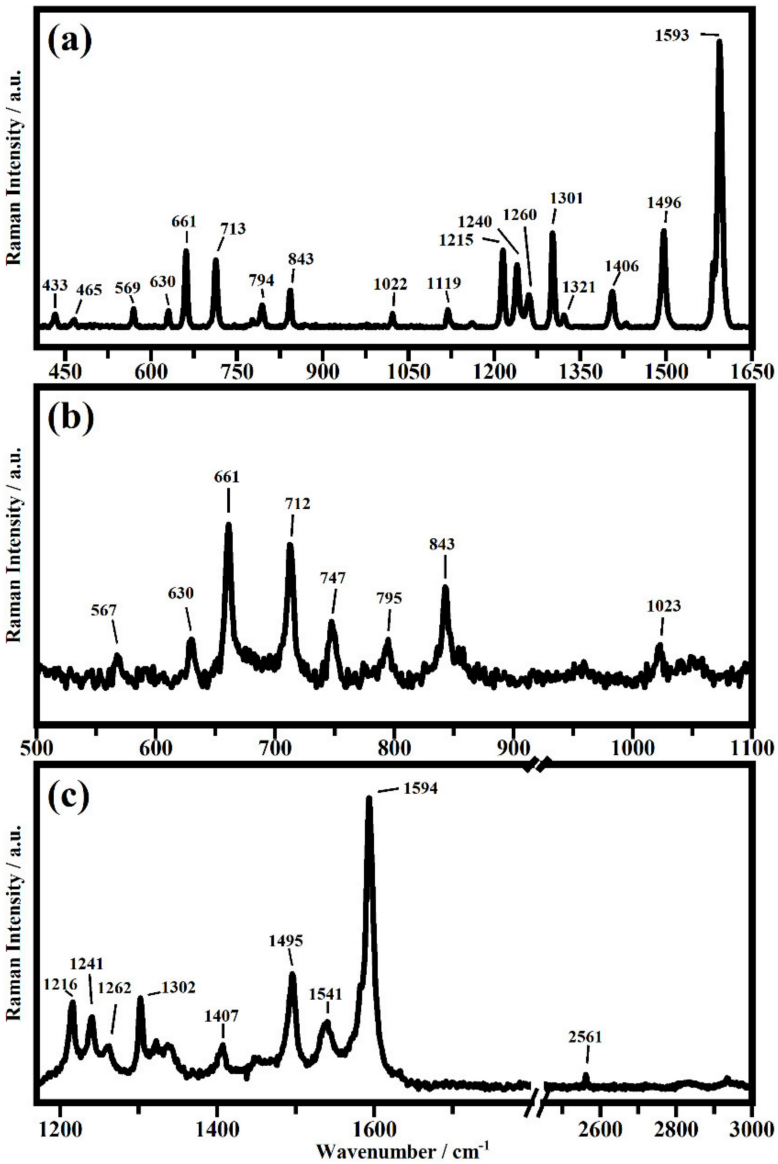

Figure 11. The first representative SERS spectrum of Bpy-SH@Au-plate in the range between 400 and 1650 cm^{-1} (laser source at 633 nm) (**a**) and the second representative SERS spectra of Bpy-SH@Au-plate in the ranges between 500 and 1100 cm^{-1} (**b**), 1170 and 1800 cm^{-1}, 2450 and 3000 cm^{-1} (**c**) (laser source at 633 nm).

The presence of the band associated with S-H stretching means that the SERS effect allows for the observation that the Bpy-SH layer on the gold plate in the Bpy-SH@Au-plate samples is not homogenous; in some areas, there are not thiol groups free and in others, there is the presence of free S-H groups. The explanation for such experimental evidence could be attributed to the orientation of the Bpy-SH molecules on the plate. When the S-H groups are detectable, the molecules of Bpy-SH are perpendicularly bonded to the gold surface and one of two thiols group remains free. On the areas where the S-H stretching is not visible (Figure 11), the Byp-SH molecules are bonded in parallel to the gold surface.

Figure 12 reports the representative Raman spectrum of Bpy-SH@AuNR in water solution, collected in the 400–1800 cm^{-1} range (in the other ranges there are no detectable Raman features).

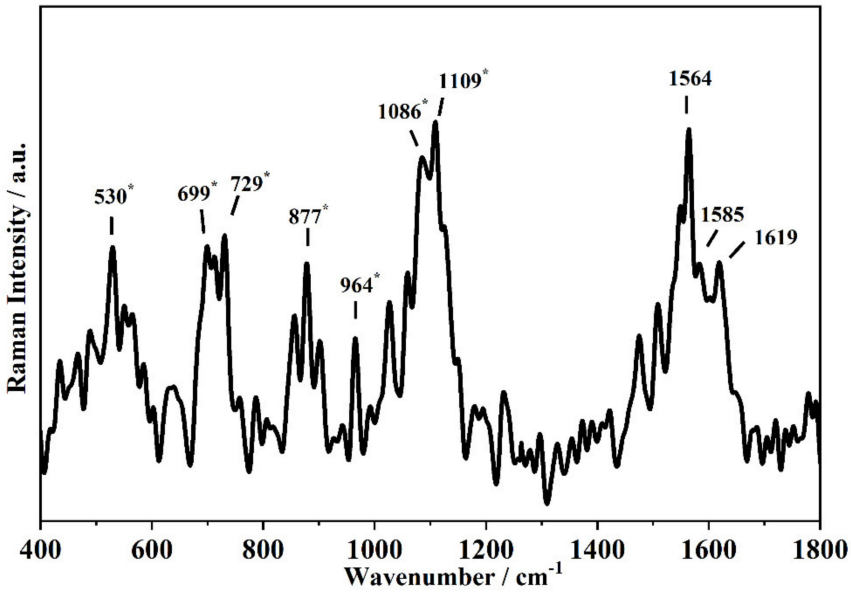

Figure 12. Raman spectrum of Bpy-SH@AuNR in water solution, collected in the 400–1800 cm^{-1} range (laser source at 532 nm). The peak indicated with the symbol "*" as an apex is assigned to PEG-SH while the others to Bpy-SH.

It is interesting to see the presence of many Raman bands that are very close to those observed in the spectra collected from the $AuNR_{PEG-SH}$ water sample (Figures S9 and S10 and Table S2 in Supplementary Materials): 530, 699, 729, 877, 964, 1086, and 1109 cm^{-1}. In addition to those Raman bands, the spectrum shows other bands at 1564, 1585, and 1619 cm^{-1} that are ascribed to the ring and C–N bond stretching of Bpy-SH deposited on the nanorods and become detectable for the SERS effect induced by the gold nanorods. Of course, it is well known that the solvent used in the last sample (water) has a very low Raman cross section. For this reason, the Raman signals coming from the nanoparticles are not covered by the Raman of the solvent [56–61].

4. Conclusions

Self-assembled monolayers are a key technology, not only because of their wide fields of application, but also because they constitute a fundamental research topic for the understanding of interfacial systems: shedding light on the wettability, electrostatic nature, and interaction properties of surfaces. SAMs are a prototypical form of nanotechnology; since they determine the interfacial properties of surfaces and nanostructures are predominantly "all surface", they are broadly useful when combined with metal nanoparticles. On the other hand, the great versatility with which it is possible to obtain different shapes of metal nanoparticles allows for the control of the formation of SAMs through careful tuning of the nanosurfaces' curvature.

In this work, for the first time, we used fluorescence to study SAM formation on gold nanoparticles in correlation with the nanosurface curvature by preparing spherical, rod-shaped, and triangular nanoparticles. Fluorescence spectroscopy, as an investigation technique, was successful as we have used a thiolated bipyridine as SAM brick molecule, whose emission wavelength and excited-state lifetime depend on the formation of close-contact ππ-stacked aggregates. When such aggregates are formed, the emission wavelength undergoes a considerable redshift accompanied by a decrease in the lifetime of the excited states.

Bpy-SH was carefully selected to have a methylene group between the terminal sulfured and the aromatic ring, considering that an SH group directly linked to the pyridine ring could have favored an electron transfer from the gold core to the chromophore, interfering with its photophysics. On the other hand, a longer aliphatic chain could have

favored Bpy-SH to deposit on the nanosurface (using both thiol terminals to bind to gold) preventing efficient $\pi\pi$ stacking in this case.

We have shown that on the faces of nanotriangles Bpy-SH molecules form highly compact SAMs, since the flat nanosurface allows the bipyridines to form $\pi\pi$-stacking interactions; on curved nanosurfaces, such as 18 nm diameter nanospheres, this is not possible. For nanorods, the observed spectral features can be ascribed to both stacked and isolated Bpy-SH, due to the functionalization of both the tips (which have a curvature similar to that of the spheres) and the sides (which are comparable to the faces of the nanotriangles). Since the use of fluorescence spectroscopy is an innovative technique for the detection of SAMs formed on gold nanoparticles, we performed a Raman spectroscopy investigation on the Bpy-SH functionalized nanosurfaces, since this is a technique already used to study SAMs on macro surfaces.

In this work, the attribution of the Raman spectra observed on the Bpy-SH powder has been propoosed. A SERS effect induced by gold nanorods and a gold plate has been shown on the Bpy-SH, with the characteristic ring stretching mode at about 1595 cm^{-1} seen in both the systems. Moreover, it has been shown that the Bpy-SH molecules are most likely bonded in two different ways: parallel to the gold surface (Figure 11) and perpendicularly to the surface (Figure 12). By exploiting the SERS effect due to the plasmonic field of the nanoparticles, the obtained outcome confirms what has been observed through the luminescence techniques.

The results obtained from these SAM@AuNPs are very encouraging, as they show a possibility of studying SAM formation using fluorescence spectroscopy and confirming the correlation between the curvature of a nanosurface and the growth of SAMs. This understanding can help to improve the properties of nanoparticles, such as stability and dispersibility, consolidating their use as platforms for the delivery of biomolecules and other therapeutic agents.

Supplementary Materials: The following supporting information can be downloaded at: https://www.mdpi.com/article/10.3390/chemosensors10050176/s1, Figure S1: Extinction spectrum of $AuNR_{CTAB}$ in water (black line) and of $AuNR_{PEG\text{-}SH}$ in dichloromethane (red line). Figure S2: Extinction spectrum of $AuNS_{SC}$ in water. Figure S3: TEM images of the obtained nanoparticles (see Section 2.3 in the main text) before the selective precipitation (a); after precipitation: supernatant (b) and precipitate (c). Figure S4: Extinction spectra of nanoparticles solutions before the selective precipitation (red line); after precipitation: supernatant (blue line) and precipitate (black line) containing $AuNT_{CTAC}$ purified nanoparticles (see Figure S3 for the correspondent TEM image). Figure S5: Absorption spectrum of Bpy-SH in diluted dichloromethane solution (1.3×10^{-5} M). Figure S6: Absorption spectrum of 2,2′-bipyridine in diluted dichloromethane solution (1.3×10^{-5} M). Figure S7: Emission spectra of Bpy-SH dichloromethane solutions at various concentrations (λ_{ex} = 306 nm). Figure S8: Excitation spectrum of **Bpy-SH@AuNR** in water solution (λ_{em} = 350 nm). Figure S9: Raman spectrum of PEG-SH in powder sample collected in the ranges between 150 and 1600 cm^{-1} and between 2400 and 3100 cm^{-1} (laser source at 532 nm). Figure S10: Raman spectrum of PEG-SH in powder sample collected in the ranges between 150 and 1600 cm^{-1} and between 2400 and 3100 cm^{-1} (laser source at 532 nm). Table S1: Raman modes attribution of Bpy-SH in powder sample. Table S2: PEG-SH Raman modes and their attribution.

Author Contributions: Synthesis and functionalization of nanoparticles, photophysical characterization, A.C. (Angela Candreva); Figures editing, F.P.; Bibliography, G.D.M. and F.S.; RAMAN investigation, A.N., C.R., R.C.B. and M.C.; Visualization and Validation, A.C. (Alessandra Crispini), N.G. and L.R.; Project administration, supervision and writing of the original draft, M.L.D. All authors have read and agreed to the published version of the manuscript.

Funding: This research was funded by the DEMETRA Project (PON ARS01_00401).

Institutional Review Board Statement: Not applicable.

Informed Consent Statement: Not applicable.

Data Availability Statement: Data are contained within the article.

Acknowledgments: The authors thank R. Termine (CNR Nanotec) for the preparation of gold substrates on silicon wafers. Angela Candreva is grateful to Luis Liz-Marzan (Ikerbasque Research Professor, Scientific Director at CIC biomaGUNE- San Sebastián, Spain) for welcoming her into his laboratory and for mentoring her in nanoparticle synthesis techniques.

Conflicts of Interest: The authors declare no conflict of interest.

References

1. Ulman, A. Formation and Structure of Self-Assembled Monolayers. *Chem. Rev.* **1996**, *96*, 1533–1554. [CrossRef] [PubMed]
2. Schreiber, F. Structure and Growth of Self-Assembling Monolayers. *Prog. Surf. Sci.* **2000**, *65*, 151–257. [CrossRef]
3. Kühnle, A. Self-Assembly of Organic Molecules at Metal Surfaces. *Curr. Opin. Colloid Interface Sci.* **2009**, *14*, 157–168. [CrossRef]
4. Chaki, N.K.; Vijayamohanan, K. Self-Assembled Monolayers as a Tunable Platform for Biosensor Applications. *Biosens. Bioelectron.* **2002**, *17*, 1–12. [CrossRef]
5. Motealleh, A.; Dorri, P.; Kehr, N.S. Self-Assembled Monolayers of Chiral Periodic Mesoporous Organosilica as a Stimuli Responsive Local Drug Delivery System. *J. Mater. Chem. B* **2019**, *7*, 2362–2371. [CrossRef]
6. Gankin, A.; Mervinetsky, E.; Alshanski, I.; Buchwald, J.; Dianat, A.; Gutierrez, R.; Cuniberti, G.; Sfez, R.; Yitzchaik, S. ITO Work Function Tunability by Polarizable Chromophore Monolayers. *Langmuir* **2019**, *35*, 2997–3004. [CrossRef]
7. Love, J.C.; Estroff, L.A.; Kriebel, J.K.; Nuzzo, R.G.; Whitesides, G.M. Self-Assembled Monolayers of Thiolates on Metals as a Form of Nanotechnology. *Chem. Rev.* **2005**, *105*, 1103–1170. [CrossRef]
8. Laibinis, P.E.; Whitesides, G.M.; Allara, D.L.; Tao, Y.T.; Parikh, A.N.; Nuzzo, R.G. Comparison of the Structures and Wetting Properties of Self-Assembled Monolayers of n-Alkanethiols on the Coinage Metal Surfaces, Copper, Silver, and Gold. *J. Am. Chem. Soc.* **1991**, *113*, 7152–7167. [CrossRef]
9. Heister, K.; Allara, D.L.; Bahnck, K.; Frey, S.; Zharnikov, M.; Grunze, M. Deviations from 1:1 Compositions in Self-Assembled Monolayers Formed from Adsorption of Asymmetric Dialkyl Disulfides on Gold. *Langmuir* **1999**, *15*, 5440–5443. [CrossRef]
10. Hamoudi, H.; Esaulov, V.A. Selfassembly of α,ω-Dithiols on Surfaces and Metal Dithiol Heterostructures. *Ann. Phys.* **2016**, *528*, 242–263. [CrossRef]
11. Hamoudi, H. Bottom-up Nanoarchitectonics of Two-Dimensional Freestanding Metal Doped Carbon Nanosheet. *RSC Adv.* **2014**, *4*, 22035–22041. [CrossRef]
12. Hamoudi, H.; Prato, M.; Dablemont, C.; Cavalleri, O.; Canepa, M.; Esaulov, V.A. Self-Assembly of 1,4-Benzenedimethanethiol Self-Assembled Monolayers on Gold. *Langmuir* **2010**, *26*, 7242–7247. [CrossRef] [PubMed]
13. Pethkar, S.; Aslam, M.; Mulla, I.S.; Ganeshan, P.; Vijayamohanan, K. Preparation and Characterisation of Silver Quantum Dot Superlattice Using Self-Assembled Monolayers of Pentanedithiol. *J. Mater. Chem.* **2001**, *11*, 1710–1714. [CrossRef]
14. Sarathy, K.V.; Thomas, P.J.; Kulkarni, G.U.; Rao, C.N.R. Superlattices of Metal and Metal-Semiconductor Quantum Dots Obtained by Layer-by-Layer Deposition of Nanoparticle Arrays. *J. Phys. Chem. B* **1999**, *103*, 399–401. [CrossRef]
15. Jackson, A.M.; Myerson, J.W.; Stellacci, F. Spontaneous Assembly of Subnanometre-Ordered Domains in the Ligand Shell of Monolayer-Protected Nanoparticles. *Nat. Mater.* **2004**, *3*, 330–336. [CrossRef] [PubMed]
16. Eustis, S.; El-Sayed, M.A. Why Gold Nanoparticles Are More Precious than Pretty Gold: Noble Metal Surface Plasmon Resonance and Its Enhancement of the Radiative and Nonradiative Properties of Nanocrystals of Different Shapes. *Chem. Soc. Rev.* **2006**, *35*, 209–217. [CrossRef]
17. Lu, W.; Suo, Z. Symmetry Breaking in Self-Assembled Monolayers on Solid Surfaces: Anisotropic Surface Stress. *Phys. Rev. B* **2002**, *65*, 085401. [CrossRef]
18. Häkkinen, H. The gold–sulfur interface at the nanoscale. *Nat. Chem.* **2012**, *4*, 443–455. [CrossRef]
19. Liang, J.; Rosa, L.G.; Scoles, G. Nanostructuring, Imaging and Molecular Manipulation of Dithiol Monolayers on Au(111) Surfaces by Atomic Force Microscopy. *J. Phys. Chem. C* **2007**, *111*, 17275–17284. [CrossRef]
20. Rieley, H.; Kendall, G.K.; Zemicael, F.W.; Smith, T.L.; Yang, S. X-ray Studies of Self-Assembled Monolayers on Coinage Metals. 1. Alignment and Photooxidation in 1,8-Octanedithiol and 1-Octanethiol on Au. *Langmuir* **1998**, *14*, 5147–5153. [CrossRef]
21. De Luca, O.; Caruso, T.; Turano, M.; Ionescu, A.; Godbert, N.; Aiello, I.; Ghedini, M.; Formoso, V.; Agostino, R.G. Adsorption of Nile Red Self-Assembled Monolayers on Au (111). *Langmuir* **2019**, *35*, 14761–14768. [CrossRef] [PubMed]
22. Lakowicz, J.R. *Principles of Fluorescence Spectroscopy*, 3rd ed.; Springer: New York, NY, USA, 2006.
23. Mei, J.; Leung, N.L.C.; Kwok, R.T.K.; Lam, J.W.Y.; Tang, B.Z. Aggregation-Induced Emission: Together We Shine, United We Soar! *Chem. Rev.* **2015**, *115*, 11718–11940. [CrossRef] [PubMed]
24. Scarpelli, F.; Ionescu, A.; Aiello, I.; La Deda, M.; Crispini, A.; Ghedini, M.; Brunelli, E.; Sesti, S.; Godbert, N. High Order in a Self-Assembled Iridium(III) Complex Gelator Towards Nanostructured IrO_2 Thin Films. *Chem.-Asian J.* **2018**, *12*, 2703–2710. [CrossRef] [PubMed]
25. Yin, K.; Lu, D.; Tian, W.; Zhang, R.; Yu, H.; Gorecka, E.; Pociecha, D.; Godbert, N.; Hao, J.; Li, H. Ordered structures of alkylated carbon dots and their applications in nonlinear optics. *J. Mater. Chem. C* **2020**, *8*, 8980–8991. [CrossRef]
26. Li, X.; Li, Q.; Wang, Y.; Quan, Y.; Chen, D.; Cheng, Y. Strong Aggregation-Induced CPL Response Promoted by Chiral Emissive Nematic Liquid Crystals (N*-LCs). *Chem. Eur. J.* **2018**, *24*, 12607–12612. [CrossRef]

27. Galyametdinov, Y.G.; Knyazev, A.A.; Dzhabarov, V.I.; Cardinaels, T.; Driesen, K.; Görller-Walrand, C.; Binnemans, K. Polarized Luminescence from Aligned Samples of Nematogenic Lanthanide Complexes. *Adv. Mater.* **2008**, *20*, 252–257. [CrossRef]
28. Agina, E.V.; Mannanov, A.A.; Sizov, A.S.; Vechter, O.; Borshchev, O.V.; Bakirov, A.V.; Shcherbina, M.A.; Chvalun, S.N.; Konstantinov, V.G.; Bruevich, V.V.; et al. Luminescent Organic Semiconducting Langmuir Monolayers. *ACS Appl. Mater. Interfaces* **2017**, *9*, 18078–18086. [CrossRef]
29. Yokota, H.; Okazaki, K.; Shimura, K.; Nakayama, M.; Kim, D. Photoluminescence Properties of Self-Assembled Monolayers of CdSe and CdSe/ZnS Quantum Dots. *J. Phys. Chem. C* **2012**, *116*, 5456–5459. [CrossRef]
30. Séro, L.; Sanguinet, L.; Derbré, S.; Boury, F.; Brotons, G.; Dabos-Seignon, S.; Richomme, P.; Séraphin, D. Fluorescent Self-Assembled Monolayers of Umbelliferone: A Relationship between Contact Angle and Fluorescence. *Langmuir* **2013**, *29*, 10423–10431. [CrossRef]
31. Sun, S.-S.; Lees, A.J. Photophysics and Evidence of Excimer Formation, Linear Bipyridines in Solution and Solid Films. *J. Photochem. Photobiol. A* **2001**, *140*, 157–161. [CrossRef]
32. Scarabelli, L.; Grzelczak, M.; Liz-Marzán, L.M. Tuning Gold Nanorod Synthesis through Prereduction with Salicylic Acid. *Chem. Mater.* **2013**, *25*, 4232–4238. [CrossRef]
33. Candreva, A.; Lewandowski, W.; La Deda, M. Thickness control of the silica shell: A way to tune the plasmonic properties of isolated and assembled gold nanorods. *J. Nanopart. Res.* **2021**, *24*, 19. [CrossRef]
34. Liu, Q.; Yuan, Y.; Smalyukh, I.I. Electrically and Optically Tunable Plasmonic Guest–Host Liquid Crystals with Long-Range Ordered Nanoparticles. *Nano Lett.* **2014**, *14*, 4071–4077. [CrossRef] [PubMed]
35. Scarabelli, L.; Coronado-Puchau, M.; Giner-Casares, J.J.; Langer, J.; Liz-Marzán, L.M. Monodisperse Gold Nanotriangles: Size Control, Large-Scale Self-Assembly, and Performance in Surface-Enhanced Raman Scattering. *ACS Nano* **2014**, *8*, 5833–5842. [CrossRef] [PubMed]
36. Sakotsubo, Y.; Ohgi, T.; Fujita, D.; Ootuka, Y. Tunneling Spectroscopy of Isolated Gold Clusters Grown on Thiol/Dithiol Mixed Self-Assembled Monolayers. *Phys. E Low-Dimens. Syst. Nanostruct.* **2005**, *29*, 601–605. [CrossRef]
37. Bastús, N.G.; Comenge, J.; Puntes, V. Kinetically Controlled Seeded Growth Synthesis of Citrate-Stabilized Gold Nanoparticles of up to 200 Nm: Size Focusing versus Ostwald Ripening. *Langmuir* **2011**, *27*, 11098–11105. [CrossRef]
38. Gao, M.; Zheng, X.; Khan, I.; Cai, H.; Lan, J.; Liu, J.; Wang, J.; Wu, J.; Huang, S.; Li, S.; et al. Resonant Light Absorption and Plasmon Tunability of Lateral Triangular Au Nanoprisms Array. *Phys. Lett. A* **2019**, *383*, 125881. [CrossRef]
39. Battistini, G.; Cozzi, P.G.; Jalkanen, J.-P.; Montalti, M.; Prodi, L.; Zaccheroni, N.; Zerbetto, F. The Erratic Emission of Pyrene on Gold Nanoparticles. *ACS Nano* **2008**, *2*, 77–84. [CrossRef]
40. Dulkeith, E.; Morteani, A.C.; Niedereichholz, T.; Klar, T.A.; Feldmann, J.; Levi, S.A.; van Veggel, F.C.J.M.; Reinhoudt, D.N.; Möller, M.; Gittins, D.I. Fluorescence Quenching of Dye Molecules near Gold Nanoparticles: Radiative and Nonradiative Effects. *Phys. Rev. Lett.* **2002**, *89*, 203002. [CrossRef]
41. Candreva, A.; Di Maio, G.; La Deda, M. A Quick One-Step Synthesis of Luminescent Gold Nanospheres. *Soft Matt.* **2020**, *16*, 10865–10868. [CrossRef]
42. De Luca, A.; Ferrie, M.; Ravaine, S.; La Deda, M.; Infusino, M.; Rashed, A.R.; Veltri, A.; Aradian, A.; Scaramuzza, N.; Strangi, G. Gain Functionalized Core-Shell Nanoparticles: The Way to Selectively Compensate Absorptive Losses. *J. Mater. Chem.* **2012**, *22*, 8846–8852. [CrossRef]
43. Scarpelli, F.; Ionescu, A.; Ricciardi, L.; Plastina, P.; Aiello, I.; la Deda, M.; Crispini, A.; Ghedini, M.; Godbert, N. A novel route towards water-soluble luminescent iridium(III) complexes via a hydroxy-bridged dinuclear precursor. *Dalton Trans.* **2016**, *45*, 17264–17273. [CrossRef] [PubMed]
44. Liguori, P.F.; Ghedini, M.; la Deda, M.; Godbert, N.; Parisi, F.; Guzzi, R.; Ionescu, A.; Aiello, I. Electrochromic behaviour of Ir(III) bis-cyclometalated 1,2-dioxolene tetra-halo complexes: Fully reversible catecholate/semiquinone redox switches. *Dalton Trans.* **2020**, *49*, 2628–2635. [CrossRef] [PubMed]
45. Ionescu, A.; Caligiuri, R.; Godbert, N.; Candreva, A.; la Deda, M.; Furia, E.; Ghedini, M.; Aiello, I. New electropolymerizable Ir(III) complexes with β-ketoiminate ancillary ligands. *Chem. Asian J.* **2019**, *14*, 3025–3034. [CrossRef]
46. Mutai, T.; Cheon, J.D.; Tsuchiya, G.; Araki, K. Tuning of fluorescence properties of aminopyridine*** fluorophores by N-substitution. *J. Chem. Soc. Perkin Trans. 2* **2002**, *2*, 862–865. [CrossRef]
47. Poizat, O.; Buntinx, G.; Valat, P.; Wintgens, V.; Bridoux, M. Photochemistry of 4,4′-Bipyridine. Nanosecond Absorption and Raman Study of the Hydrogen Atom Abstraction from Methanol and 2-Propanol. *J. Phys. Chem.* **1993**, *97*, 5905–5910. [CrossRef]
48. Gao, X. Reproducibility in Surface-Enhanced Raman Spectroscopy. *J. Phys. Chem.* **1990**, *94*, 6858–6864. [CrossRef]
49. Ducasse, L.; Dussauze, M.; Grondin, J.; Lassègues, J.C.; Naudin, C.; Servant, L. Spectroscopic study of poly(ethylene oxide)$_6$: LiX complexes (X = PF_6, AsF_6, SbF_6, ClO_4). *Phys. Chem. Chem. Phys.* **2003**, *5*, 567–574. [CrossRef]
50. Gupta, R.; Dyer, M.J.; Weimer, W.A. Preparation and characterization of surface plasmon resonance tunable gold and silver films. *J. Appl. Phys.* **2002**, *92*, 5264–5271. [CrossRef]
51. Yang, T.; Long, H.; Malkoch, M.; Gamstedt, E.K.; Berglund, L.; Hult, A. Characterization of Well-Defined Poly(ethylene glycol) Hydrogels Prepared by Thiol-ene Chemistry. *J. Polym. Sci. Part A Polym. Chem.* **2011**, *49*, 4044–4054. [CrossRef]
52. Ould-Moussa, L.; Castella-Ventura, M.; Kassab, E.; Poizat, O.; Strommen, D.P.; Kincaid, J.R. Ab initio and density functional study of the geometrical, electronic and vibrational properties of 2,2′-bipyridine. *J. Raman Spectrosc.* **2000**, *31*, 377–390. [CrossRef]

53. Kumar, J.; Thomas, R.; Swathi, R.S.; Thomas, K.G. Au nanorod quartets and Raman signal enhancement: Towards the design of plasmonic platforms. *Nanoscale* **2014**, *6*, 10454–10459. [CrossRef] [PubMed]
54. Joo, S.W.; Han, S.W.; Kim, K. Adsorption Characteristics of p-Xylene-r,r′-dithiol on Gold and Silver Surfaces: Surface-Enhanced Raman Scattering and Ellipsometry Study. *J. Phys. Chem. B* **1999**, *103*, 10831–10837. [CrossRef]
55. Kumar, J.; Thomas, K.G. Surface-Enhanced Raman Spectroscopy: Investigations at the Nanorod Edges and Dimer Junctions. *J. Phys. Chem. Lett.* **2011**, *2*, 610–615. [CrossRef]
56. Kertesz, M.; Choi, C.H.; Hong, S.Y. Conformational Information from Vibrational Spectra of Polyaniline. *Synth. Met.* **1997**, *85*, 1073–1076. [CrossRef]
57. Zhang, Z.; Lin, M. Fast loading of PEG–SH on CTAB-protected gold nanorods. *RSC Adv.* **2014**, *4*, 17760–17767. [CrossRef]
58. Serrano-Montes, A.B.; Jimenez de Aberasturi, D.; Langer, J.; Giner-Casares, J.J.; Scarabelli, L.; Herrero, A.; Liz-Marzán, L.M. A General Method for Solvent Exchange of Plasmonic Nanoparticles and Self-Assembly into SERS-Active Monolayers. *Langmuir* **2015**, *31*, 9205–9213. [CrossRef]
59. Yüce, M.; Kurt, H. How to make nanobiosensors: Surface modification and characterisation of nanomaterials for biosensing applications. *RSC Adv.* **2017**, *7*, 49386–49403. [CrossRef]
60. Conde, J.; Dias, J.T.; Grazú, V.; Moros, M.; Baptista, P.V.; de la Fuente, J.M. Revisiting 30 years of biofunctionalization and surface chemistry of inorganic nanoparticles for nanomedicine. *Front. Chem.* **2014**, *2*, 48. [CrossRef]
61. Whitney, A.V.; van Duyne, R.P.; Casadio, F. An innovative surface-enhanced Raman spectroscopy (SERS) method for the identification of six historical red lakes and dyestuffs. *J. Raman Spectrosc.* **2006**, *37*, 993–1002. [CrossRef]